

Induction Mapping of the 3D-Modulated Spin Texture of Skyrmions in Thin Helimagnets

S. Schneider,^{1,2} D. Wolf,³ M. J. Stolt,⁴ S. Jin,⁴ D. Pohl,^{1,5} B. Rellinghaus,^{1,5} M. Schmidt,⁶ B. Büchner,³ S. T. B. Goennenwein,^{2,7} K. Nielsch,^{1,8} and A. Lubk³

¹*Institute for Metallic Materials, IFW Dresden, Helmholtzstr. 20, 01069 Dresden, Germany*

²*Institut für Festkörper- und Materialphysik, Technische Universität Dresden, 01062 Dresden, Germany*

³*Institute for Solid State Research, IFW Dresden, Helmholtzstr. 20, 01069 Dresden, Germany*

⁴*Department of Chemistry, University of Wisconsin-Madison,*

1101 University Avenue, Madison, Wisconsin 53706, United States

⁵*Dresden Center for Nanoanalysis, Technische Universität Dresden, 01062 Dresden, Germany*

⁶*Department Chemical Metal Science, Max Planck Institute for Chemical*

Physics of Solids, Nöthnitzer Str. 40, 01187 Dresden, Germany

⁷*Center for Transport and Devices of Emergent Materials,*

Technische Universität Dresden, 01062 Dresden, Germany

⁸*Institute of Materials Science, Technische Universität Dresden, Helmholtzstr. 7, 01069 Dresden, Germany*

Envisaged applications of skyrmions in magnetic memory and logic devices crucially depend on the stability and mobility of these topologically non-trivial magnetic textures in thin films. We present for the first time quantitative maps of the magnetic induction that provide evidence for a 3D modulation of the skyrmionic spin texture. The projected in-plane magnetic induction maps as determined from in-line and off-axis electron holography carry the clear signature of Bloch skyrmions. However, the magnitude of this induction is much smaller than the values expected for homogeneous Bloch skyrmions that extend throughout the thickness of the film. This finding can only be understood, if the underlying spin textures are modulated along the out-of-plane z direction. The projection of (the in-plane magnetic induction of) helices is further found to exhibit thickness-dependent lateral shifts, which show that this z modulation is accompanied by an (in-plane) modulation along the x and y directions.

I. INTRODUCTION

Skyrmions [1] are topologically non-trivial vortex-like spin textures, anticipated for application in spintronic technologies, referred to as skyrmionics, in next generation magnetic data processing and storage due to their facile manipulation by spin-polarized currents of very low magnitude [2, 3]. The unique features of skyrmions, e.g., their dynamics, topological structure, competing magnetic interactions, are generally of great interest from a fundamental physics point, understanding emerging magnetic field-like interactions induced by topologically non-trivial chiral spin structures. In chiral-lattice ferromagnets without spatial inversion symmetry, such as the B20 compound $\text{Fe}_{0.95}\text{Co}_{0.05}\text{Ge}$ (see Fig. 1 (a)) investigated in this work, skyrmions arise from the interplay between the Dzyaloshinskii-Moriya interaction [4, 5] and ferromagnetic exchange mechanisms [6]. Indeed, these and similar competing interactions, such as surface dipolar interaction, may lead to a whole zoo of non-trivial spin textures, including helical, cycloidal and various skyrmionic phases (antiskyrmions [7], Néel skyrmions [8]). Besides spin-polarized STM [9] and MFM [10] probing the surface spin texture, X-ray microscopy [11] was used to investigate the projected magnetic structure of skyrmions. Furthermore Lorentz transmission electron microscopy (TEM) and transport of intensity (TIE) holography have been employed to reveal the projected skyrmionic texture in a variety of studies [12–15] in dependency of the applied magnetic field, temperature, sample thickness and

crystallographic orientation, covering a large class of materials.

However, in particular for skyrmionics, knowledge about the full three-dimensional spin texture including its coupling to surfaces and interfaces, ubiquitous in thin film technology, is of fundamental importance, because it determines the stability and dynamics of the skyrmion state. Several theoretic studies predicted the occurrence of 3D modulated skyrmion textures [16–19] as a consequence of surface anisotropies as well as 3D Dzyaloshinskii-Moriya interaction, also taking into account similarities to smectic liquid crystals [20, 21]. In particular, Rybakov, Borisov and Bogdanov theoretically predicted the presence of a chiral surface twist [16], which was later experimentally discovered in epilayers of chiral magnets [22, 23]. This surface modulation renders the skyrmionic state stable in thin film geometries (making it a ground state) as opposed to its metastable (i.e., excited) nature in the bulk. Later, a full-blown phase diagram of helical, skyrmionic, and other magnetic textures, such as Bobbers [24] has been computed for thin films of isotropic chiral magnets [19]. Experimental studies on modulated 3D spin textures in skyrmions have been, however, elusive to date. Similarly, almost none of the abundant microscopy studies [12–15, 25–28] give quantitative values of projected magnetic fields carrying a fingerprint of the modulated 3D texture to the best knowledge of the authors.

Here, we seek to fill this gap by carrying out electron holography (EH) studies at different orientations of the

sample to quantitatively reconstruct the projected magnetic field pertaining to both the helical and the skyrmion lattice phase in single crystal nanoplates of the isotropic chiral magnet $\text{Fe}_{0.95}\text{Co}_{0.05}\text{Ge}$. We compare our experimental results to magnetostatic simulations taking into account 3D modulation models such the chiral surface twist in order to discuss the presence of 3D spin textures in skyrmions. Our findings clearly suggest (i) the presence of inhomogeneous spin textures similar to previously discussed surface modulations and (ii) show that currently available spin structure models cannot account for our experimental results.

II. FUNDAMENTALS

Following [29] one may describe the isotropic chiral magnet FeGe (space group $P2_13$) with a continuum spin model (normalized magnetization vector \mathbf{m}), i.e., as a (meta)stable state of the free energy

$$F \propto \int \left(J \left(|\nabla m_x|^2 + |\nabla m_y|^2 + |\nabla m_z|^2 \right) + D\mathbf{m} \cdot (\nabla \times \mathbf{m}) - \mathbf{H}\mathbf{m}M_s \right) d^3r, \quad (1)$$

the interplay of ferromagnetic exchange and the Dzyaloshinskii-Moriya interaction leads to the formation of a helical spin order with a periodicity $L_D = 4\pi J/D$ determined by the ratio of the Dzyaloshinskii-Moriya interaction constant D and the ferromagnetic exchange interaction constant J ($L_D \approx 70 \text{ nm}$ in FeGe [30]). When additionally applying a weak magnetic field below the critical field $H_D = D^2/(2M_S J)$ skyrmions typically arrange in a hexagonal lattice formed by three superimposing helical spin waves appearing in a plane normal to the field irrespective of the crystal orientation due to the weak crystal anisotropy in FeGe.

In addition, it is well-known that the stability of a skyrmion state increases as the thickness of the FeGe sample decreases [13]. Recently, a 3D modulation of the spin texture of the helical and Skyrmion phase with a chiral surface twist was predicted [16, 17, 19], which stabilizes the skyrmionic state in thin films. The proposed 3D texture can be described by the z -invariant helical spiral modulated by an additional azimuthal modulation of the magnetization, $\psi = \sin L_D z$, which resembles to add a Néel type magnetic texture close to the surfaces [19]. Note, however, that the predicted length of the chiral surface twist is rather small ($< L_D/4$), rendering its experimental observation challenging. Furthermore, little is known about additional possible surface modulations, e.g., induced by surface anisotropies. Another layer of complexity is introduced by surface modulations occurring during the fabrication of thin magnetic layers. For instance, surface damage during synthesis or TEM specimen preparation may lead to a non-magnetic layer.

III. EXPERIMENTAL

In order to experimentally probe the 3D modulation of magnetic textures we apply focal series in-line and off-axis EH enabling the reconstruction of the projections of the lateral components of the magnetic induction $\int \mathbf{B}_\perp dz$, respectively (see the Supplemental Material, Suppl. I). This implies that cycloidal modulations (and hence also Néel skyrmions) are invisible in these techniques, if they are aligned perpendicular to the beam, because the stray fields above and below the thin film sample cancel the lateral fields within the sample in projection. Thus, to observe cycloidal modulation the specimen needs to be tilted with respect to the electron beam.

The skyrmion phase was investigated using a double corrected FEI Titan³ 80-300 microscope operated in imaging corrected Lorentz mode (conventional objective lens turned off) at an acceleration voltage of 300 kV. All measurements were performed at a sample temperature of 90 K using a Gatan double tilt liquid nitrogen cooling holder. Since artifacts implemented during the sample preparation in the standard FIB preparation of thin TEM lamellas may alter the magnetic properties of the thin film, we investigated as-synthesized $\text{Fe}_{0.95}\text{Co}_{0.05}\text{Ge}$ particles (see the Supplemental Material, Suppl. II). For TEM investigations, the particles were transferred onto a holey carbon film by swiping the TEM grid gently over the particles on top of the Ge substrate. An applied field of 43 mT in out-of-plane direction leads to the appearance of the skyrmion phase in the slab-like $\text{Fe}_{0.95}\text{Co}_{0.05}\text{Ge}$ nanoplate (see Fig. 1 (d)). A focal series of Lorentz TEM (L-TEM) images ranging from +840 μm to -840 μm in focus steps of 84 μm of a single isolated nanoplate oriented along [001] zone axis (see Fig. 1 (b)) was recorded. Reconstruction of the electron wave's phase and hence the magnetic induction was obtained with the help of a modified Gerchberg-Saxton type algorithm incorporating affine image registration due to magnification change and residual shifts as well as rotations building up in such a long range focal series [31].

To supplement the focal series reconstructions from large field of views (eventually suffering from a damping of very low and large spatial frequencies [31]), smaller areas of the same nanoplate were investigated by off-axis EH [32]. To this end, the electron biprism voltage was set to 180 V to produce an overlap interference width of 500 nm and a holographic interference fringe spacing of 1.4 nm. For hologram recording, an exposure time of 4 s was employed. Off-axis electron holograms were reconstructed numerically using a standard Fourier transform based method with sideband filtering using in-house developed scripts for Gatan Microscopy Suite (GMS) software package. Contour lines and colour maps were generated from recorded magnetic phase images to yield magnetic induction maps (see the Supplemental Material, Suppl. III). The sample thickness was determined by means of zero-loss energy-filtered (EF)TEM using a Gatan Tridiem 865 energy filter yielding a thickness

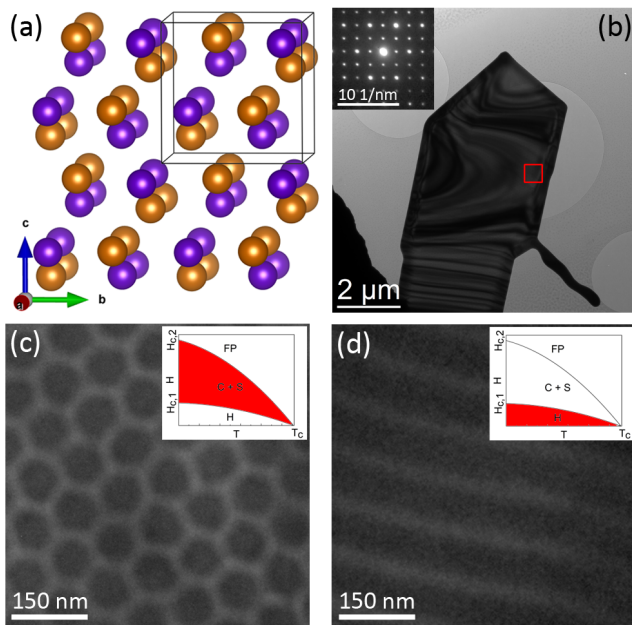


Figure 1. (a) Structure of FeGe and Fe_{0.95}Co_{0.05}Ge in the cubic B20 phase. Fe and Co atoms are shown in violet and Ge in brown. (b) TEM image of a Fe_{0.95}Co_{0.05}Ge nanoplate in [001] orientation on a holey carbon support with the diffraction pattern shown in the inset. The red square marks the area investigated by L-TEM and EH. (c) Skyrmion lattice and (d) helical phase as observed within the marked area in panel (a) in fields of 43 mT and 0 mT, respectively. The insets show schematically the magnetic phase diagrams with the corresponding phases marked in red. H, C, S, and FP denote the helical, cycloidal, skyrmion or field polarized ferromagnetic phases, respectively.

wedge over the field of view between 100 nm and 150 nm in the case of in-line EH as well as between 100 nm and 200 nm in the case of off-axis EH. In the latter case, the thickness measurement was confirmed by using the phase image (see the Supplemental Material, Suppl. IV).

To reveal the z -modulation, we recorded a EH tilt series of the helical phase of the previously investigated nanoplate ranging from -40° to $+30^\circ$ without magnetic field applied at both temperatures 90 K and room temperature (see the Supplemental Material, Suppl. V). Higher tilt angles could not be attained because of technical limitations of the liquid nitrogen cooling holder. We reduced dynamical diffraction contrast by tilting the specimen -7° out of the [001] zone axis in direction perpendicular to the TEM goniometer axis. In order to extract 3D information from the limited tilt range of projections, we compare the tomographic data to projected magnetic fields obtained from magnetostatic simulations (see the Supplemental Material, Suppl. VII). Hereby, we take into account several z -dependent spin modulations, such as a non-magnetic surface layer or a chiral surface twist. The z -invariant case (i.e., surface layer thickness equal zero) is thereby used as reference.

IV. RESULTS

Fig. 2 (a) depicts a L-TEM micrograph in underfocus showing the hexagonal skyrmion lattice as dark contrast, which is one image of the focal series used for in-line holography reconstruction of the object exit wave in amplitude and phase (see Sect. III for acquisition and reconstruction parameters). The projected in-plane components of magnetic induction ($\mathbf{B}_\perp^{\text{proj}}(x, y)$) were computed from the spatial derivative of the reconstructed phase image (Supplemental Material, Eq. (2)). The knowledge of the projected thickness, which we determined by zero-filtered EFTEM, enables us to compute the $\mathbf{B}_\perp(x, y)$ components averaged along z -direction, i.e., $\overline{\mathbf{B}}_\perp(x, y)$. Figs. 2 (b,c) show magnetic induction maps $\overline{\mathbf{B}}_\perp(x, y)$ in cylindrical coordinate representation visualizing the spin texture of the skyrmions by $\overline{B}_\phi(x, y)$ (Fig. 2 (b)) and their donut-shaped magnitude by $\overline{B}_r(x, y)$. Likewise, we observed magnetic induction maps (Figs. 2 (e,f)) from a phase image reconstructed by off-axis EH (Fig. 2 (d)) on the same Fe_{0.95}Co_{0.05}Ge nanoplate. Comparing the results of the two holographic methods, we measure a slightly higher magnetic induction $\overline{B}_r(x, y)$ with a slightly higher spatial resolution in the case of off-axis holography. However, we consistently observe a reduction of the \mathbf{B} -fields ($\overline{B}_{\text{max}} = (0.2 \dots 0.3) T$) with respect to the z -invariant case ($\overline{B}_{\text{max}} = 0.43 T$) obtained from magnetostatic simulations. Note that we observe similar reductions in a variety of FeGe samples subject to different preparation histories (e.g., as-synthesized nanocrystals, FIB lamellas). Consequently, we can exclude the presence of a non-magnetic surface layer of approximately 40 nm as the principle reduction mechanism. In order to clarify the origin of the reduced values a 3D reconstruction of the magnetic induction by means of electron holographic tomography [33] would be required. In case of the skyrmionic lattice a tomographic investigation of the 3D modulation is currently experimentally unfeasible, because this necessitates an externally applied out-of-plane magnetic field to be tilted with the sample. In the current experimental setup, the skyrmions align along the magnetic field of the objective lens which has a fixed orientation along the optical axis. In order to overcome these pertaining experimental challenges in-situ magnetic vector field application devices and auxiliary magnetic signals such as EMCD [34–37] would be helpful. In the following, we therefore resort to acquiring a tilt series of the helical phase stabilizing without applied external field. A representative holographic \mathbf{B} -field reconstruction of the helical phase is depicted in Fig. 3 (a,b). Accordingly, we observe sinusoidal modulations of the projected lateral \mathbf{B} -field component with a period of 77 nm corresponding to spiral magnetic textures aligned in plane (see the Supplemental Material, Suppl. VI). Unfortunately, upon tilting rather large local variations occur in the phase images (e.g., bending fringes visible in the inset of Fig 3 (a)) that are related to changes in the dynamic scattering conditions of the

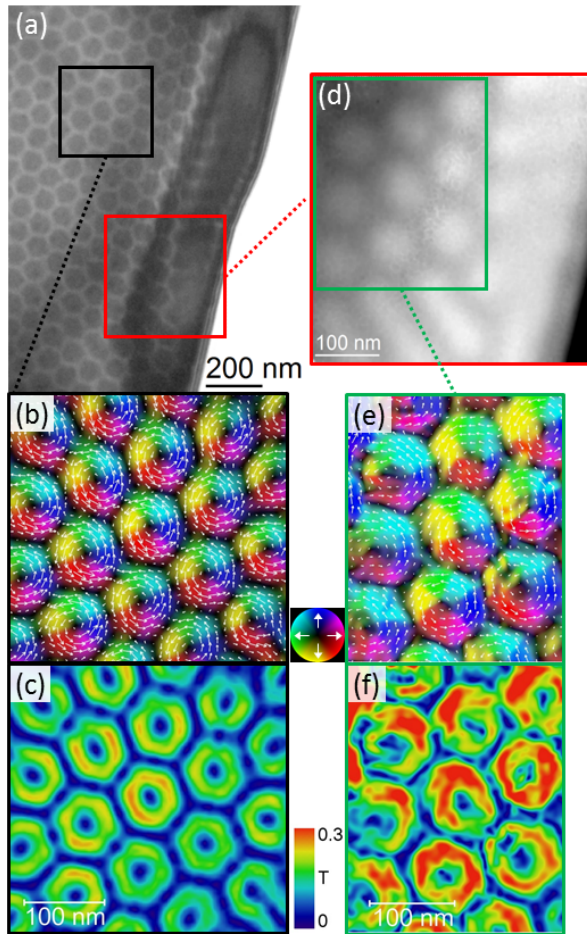


Figure 2. Reconstruction of the projected in-plane component of the magnetic induction, \mathbf{B}_\perp , within the hexagonal skyrmion lattice of the $\text{Fe}_{0.95}\text{Co}_{0.05}\text{Ge}$ nanoplatelet using in-line (a-c) and off-axis holography (d-f). (a) L-TEM image at $-84\ \mu\text{m}$ defocus showing the skyrmions as dark contrast. (d) Phase image at the position indicated by the red square in (a). (b,e) Mapping of the direction of \mathbf{B}_\perp by combining a vector plot (white arrows) and a false color image. (c,f) False colour mapping of the magnitude of \mathbf{B}_\perp .

$175\ \text{nm}$ thick crystalline sample in the region of interest (ROI). Likewise, the phase images taken at room temperature required to determine the thickness maps for each tilt, suffer from dynamical diffraction contrast and need to be treated with care (see the Supplemental Material, Suppl. V). After normalizing the projected magnetic fields with corresponding thickness maps, we consistently observe a reduction of the \mathbf{B} -fields ($\bar{B}_{\text{max}} = 0.2\ \text{T}$) with respect to the z -invariant case ($\bar{B}_{\text{max}} = 0.43\ \text{T}$) as determined in the case of the skyrmion texture. Consequently, a similar 3D modulation as for the skyrmion lattice is expected under field-free conditions.

To gain more insight in the underlying spin texture, we analyze the magnetic contrast as function of the tilt angles (Fig. 3 (c)). In the investigated nanoplatelet, the helices are aligned almost parallel to the tilt axis (mistilt

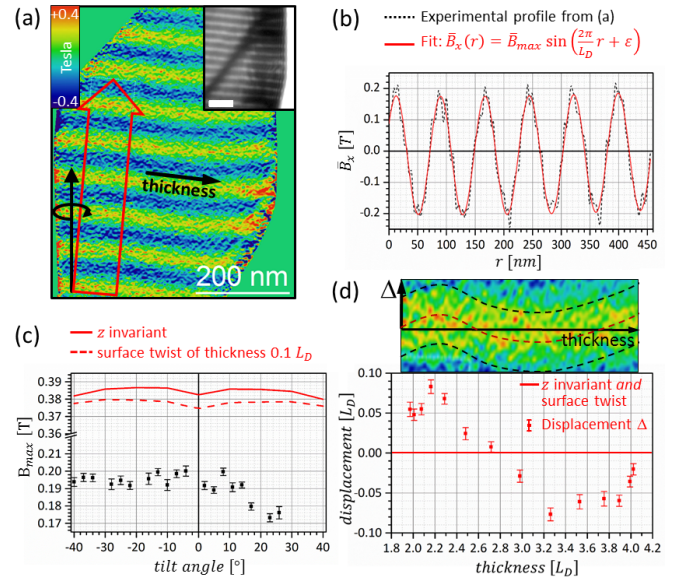


Figure 3. Dependence of the in-plane magnetic induction on the specimen tilt around the propagation axis of the helical phase in a $\text{Fe}_{0.95}\text{Co}_{0.05}\text{Ge}$ nanoplatelet. (a) In-plane component B_x (as determined from off-axis holography) normalized to the specimen thickness. The tomographic tilt axis and the direction of the thickness gradient are indicated by black arrows. The inset shows the corresponding L-TEM image (scale bar = $200\ \text{nm}$). (b) Line profile of the projected in-plane magnetic induction B_x along the red arrow (and averaged along its width) in (a) and sinusoidal fit using the function denoted above. (c) \mathbf{B} -field amplitudes \bar{B}_{max} obtained from likewise determined fits to the induction maps as function of the tilt angle. Simulations for (z -invariant) pure helical spirals (solid line) and with chiral surface twist (dashed line) are included for comparison. (d) Amplitude Δ of the undulation of the magnetic stripe contrast (perpendicular to the helical axis) around its mean value as function of the thickness in units of L_D . The anisotropically magnified stripe image shown as an example above indicates how Δ is determined. The error bars in (c) and (d) are given by the fit error.

of 5° as depicted in Fig. 3 (a)). This orientation is well-suited to identify any 3D spin modulation, such as the previously discussed mixing of helical (i.e., Bloch type) and cycloic (Néel type) spiral spin textures in the chiral surface twist, as additional contrast modulation of the stripe pattern in the tilt series. For the contrast measurement, we shifted the ROI in each phase image of the tilt series such that the same mean thickness of $175\ \text{nm}$ was achieved. This suppresses the possible influence of the thickness on the projected fields. The tilt series show a nearly constant value of \bar{B}_{max} for tilt angles from -40° to 12° and a strong drop by more than 10% at higher tilt angles. Two different scenarios have been evaluated to clarify the 3D spin configuration: (i) in case of a pure helical spiral without surface twist (solid red line) and upon tilting, the thickness-normalized fringe contrast is almost constant except for a slight modulation around zero tilt due to the above-mentioned mistilt of -7° . This

also causes a reduction of \overline{B}_{\max} from $0.43T$ to $0.38T$. (ii) Cycloic-like modulations in a surface twist layer with a thickness of $0.1L_D$ lead mainly to an additional contrast damping (dashed red line) of approximately 3% percent, which is, however, significantly smaller than experimentally observed (Fig. 3 (c)). The measured 50% reduction of the projected fields may only be explained by additional z -dependent modulations, spanning larger sections of the film. Evaluating the local fringe position (lateral phase) in a representative induction map from the tilt series (cf. Fig. 3 (a)) and correlating the latter with the corresponding thickness map, we also observed lateral in-plane displacements of the helical stripes as a function of the overall thickness (see Fig. 3 (d) and scheme above). Such an undulation points to a lateral shift of the helix as a function of the z -coordinate, which in turn would on the one hand lead to an additional contrast damping, while on the other hand, would explain the observed asymmetric dependence of the contrast on the tilt angle (Fig. 3 (c)). Such surface-related modulations of the spin texture may be stabilized by additional (surface) anisotropies in the above free energy functional.

In summary, we carried out a quantitative electron holographic reconstruction of the projected in-plane magnetic induction in $\text{Fe}_{0.95}\text{Co}_{0.05}\text{Ge}$ examined under various tilt directions. We show that these projected magnetic fields are significantly smaller than the fields expected for both z -invariant Bloch Skyrmions and the theoretic predictions of chiral surface twists in the thin

surface layers of such helimagnets. Although this finding cannot be accounted for by any present model of spin structures, it clearly shows that the underlying magnetic structure substantially deviates from that of a regular Bloch skyrmion in major sections of the film in z -direction. Analyzing the thickness dependence of the projected in-plane field pattern of the helical phase further reveals modulations of this structure also in the x - y -plane. Hence, rather than supporting the model of a homogeneous skyrmion lattice, the results of the present investigations can only be understood by assuming modulations of the skyrmionic structure in all three dimensions throughout the helimagnetic film.

ACKNOWLEDGMENTS

We thank T. Gemming for providing to us the Gatan double tilt liquid nitrogen cooling holder. The authors are indebted to A. Pöhl and T. Sturm for the preparation of the TEM samples. We thank U. Röföler, A. Leonov and A. Bogdanov for fruitful discussions. This research is supported by NSF grant ECCS-1609585. MJS also acknowledges support from the NSF Graduate Research Fellowship Program grant number DGE-1256259. AL and DW have received funding from the European Research Council (ERC) under the Horizon 2020 research and innovation programme of the European Union (grant agreement No 715620).

-
- [1] A. N. Bogdanov and A. Hubert, *Journal of Magnetism and Magnetic Materials* **138**, 255 (1994).
 - [2] N. Nagaosa and Y. Tokura, *Nature Nanotechnology* **8**, 899 (2013).
 - [3] N. Kanazawa, S. Seki, and Y. Tokura, “Noncentrosymmetric Magnets Hosting Magnetic Skyrmions,” (2017).
 - [4] I. Dzyaloshinsky, *Journal of Physics and Chemistry of Solids* **4**, 241 (1958).
 - [5] T. Moriya, *Physical Review* **120**, 91 (1960).
 - [6] W. Heisenberg, *Zeitschrift für Physik* **38**, 411 (1926).
 - [7] A. K. Nayak, V. Kumar, T. Ma, P. Werner, E. Pippel, R. Sahoo, F. Damay, U. K. Röföler, C. Felser, and S. S. P. Parkin, *Nature* **548**, 561 (2017).
 - [8] I. Kézsmárki, S. Bordács, P. Milde, E. Neuber, L. Eng, J. White, H. Rønnow, C. Dewhurst, M. Mochizuki, K. Yanai, H. Nakamura, D. Ehlers, V. Tsurkan, and A. Loidl, *Nature Materials* **14**, 1116 (2015).
 - [9] S. Heinze, K. von Bergmann, M. Menzel, J. Brede, A. Kubetzka, R. Wiesendanger, G. Bihlmayer, and S. Blügel, *Nature Physics* **7**, 713 (2011), arXiv:arXiv:1207.2331v1.
 - [10] P. Milde, D. Kohler, J. Seidel, L. M. Eng, A. Bauer, A. Chacon, J. Kindervater, S. Muhlbauer, C. Pfleiderer, S. Buhbrandt, C. Schütte, and A. Rosch, *Science* **340**, 1076 (2013), arXiv:20.
 - [11] S. Woo, K. Litzius, B. Krüger, M.-Y. Im, L. Caretta, K. Richter, M. Mann, A. Krone, R. M. Reeve, M. Weigand, P. Agrawal, I. Lemesch, M.-A. Mawass, P. Fischer, M. Kläui, and G. S. D. Beach, *Nature Materials* **15**, 501 (2016), arXiv:1502.07376.
 - [12] X. Z. Yu, Y. Onose, N. Kanazawa, J. H. Park, J. H. Han, Y. Matsui, N. Nagaosa, and Y. Tokura, *Nature* **465**, 901 (2010).
 - [13] X. Z. Yu, N. Kanazawa, Y. Onose, K. Kimoto, W. Z. Zhang, S. Ishiwata, Y. Matsui, and Y. Tokura, *Nature Materials* **10**, 106 (2011).
 - [14] S. Seki, X. Z. Yu, S. Ishiwata, and Y. Tokura, *Science* **336**, 198 (2012).
 - [15] X. Yu, J. P. DeGrave, Y. Hara, T. Hara, S. Jin, and Y. Tokura, *Nano Letters* **13**, 3755 (2013).
 - [16] F. N. Rybakov, A. B. Borisov, and A. N. Bogdanov, *Physical Review B - Condensed Matter and Materials Physics* **87**, 094424 (2013), arXiv:1212.5970.
 - [17] A. Leonov, Y. Togawa, T. Monchesky, A. Bogdanov, J. Kishine, Y. Kousaka, M. Miyagawa, T. Koyama, J. Akimitsu, T. Koyama, K. Harada, S. Mori, D. McGrouther, R. Lamb, M. Krajenak, S. McVitie, R. Stamps, and K. Inoue, *Physical Review Letters* **117**, 087202 (2016).
 - [18] A. O. Leonov, I. E. Dragunov, U. K. Röföler, and A. N. Bogdanov, *Physical Review E - Statistical, Non-linear, and Soft Matter Physics* **90**, 042502 (2014), arXiv:1407.7409.
 - [19] F. N. Rybakov, A. B. Borisov, S. Blügel, and N. S. Kiselev, *New Journal of Physics* **18**, 045002 (2016), arXiv:1601.05752.
 - [20] G. A. Hinshaw, R. G. Petschek, and R. A. Pelcovits,

- Physical Review Letters **60**, 1864 (1988).
- [21] M. Glogarová, E. Górecka, L. Leječek, and H. Sverenyák, *Molecular Crystals and Liquid Crystals Science and Technology. Section A. Molecular Crystals and Liquid Crystals* **301**, 325 (1997).
- [22] M. N. Wilson, E. A. Karhu, D. P. Lake, A. S. Quigley, S. Meynell, A. N. Bogdanov, H. Fritzsche, U. K. Röckler, and T. L. Monchesky, *Physical Review B* **88**, 214420 (2013).
- [23] S. A. Meynell, M. N. Wilson, H. Fritzsche, A. N. Bogdanov, and T. L. Monchesky, *Physical Review B* **90**, 014406 (2014).
- [24] F. Zheng, F. N. Rybakov, A. B. Borisov, D. Song, S. Wang, Z.-A. Li, H. Du, N. S. Kiselev, J. Caron, A. Kovács, M. Tian, Y. Zhang, S. Blügel, and R. E. Dunin-Borkowski, arXiv , 1706.04654 (2017), arXiv:1706.04654.
- [25] H. S. Park, X. Yu, S. Aizawa, T. Tanigaki, T. Akashi, Y. Takahashi, T. Matsuda, N. Kanazawa, Y. Onose, D. Shindo, A. Tonomura, and Y. Tokura, *Nature Nanotechnology* **9**, 337 (2014).
- [26] A. Kovács, Z.-A. Li, K. Shibata, and R. E. Dunin-Borkowski, *Resolution and Discovery* **1**, 2 (2016).
- [27] K. Shibata, A. Kovács, N. S. Kiselev, N. Kanazawa, R. E. Dunin-Borkowski, and Y. Tokura, *Physical Review Letters* **118**, 087202 (2017), arXiv:1606.05723.
- [28] C. Jin, Z.-A. Li, A. Kovács, J. Caron, F. Zheng, F. N. Rybakov, N. S. Kiselev, H. Du, S. Blügel, M. Tian, Y. Zhang, M. Farle, and R. E. Dunin-Borkowski, *Nature Communications* **8**, 15569 (2017).
- [29] A. N. Bogdanov and D. A. Yablonskii, *Zh. Eksp. Teor. Fiz.* **95**, 178 (1989).
- [30] B. Lebech, J. Bernhard, and T. Freltoft, *Journal of Physics: Condensed Matter* **1**, 6105 (1999), arXiv:arXiv:1011.1669v3.
- [31] A. Lubk, K. Vogel, D. Wolf, J. Krehl, F. Röder, L. Clark, G. Guzzinati, and J. Verbeeck, in *Advances in Imaging and Electron Physics*, Vol. 197 (Elsevier, 2016) pp. 105–147.
- [32] H. Lichte, F. Börrnert, A. Lenk, A. Lubk, F. Röder, J. Sickmann, S. Sturm, K. Vogel, and D. Wolf, *Ultramicroscopy* **134**, 126 (2013).
- [33] D. Wolf, L. A. Rodriguez, A. Beche, E. Javon, L. Serrano, C. Magen, C. Gatel, A. Lubk, H. Lichte, S. Bals, G. Van Tendeloo, A. Fernandez-Pacheco, J. M. De Teresa, and E. Snoeck, *Chemistry of Materials*, *Chemistry of Materials* **27**, 6771 (2015).
- [34] P. Schattschneider, S. Rubino, C. Hébert, J. Rusz, J. Kuneš, P. Novák, E. Carlino, M. Fabrizioli, G. Panaccione, and G. Rossi, *Nature* **441**, 486 (2006).
- [35] S. Schneider, D. Pohl, S. Löffler, J. Rusz, D. Kasinathan, P. Schattschneider, L. Schultz, and B. Rellinghaus, *Ultramicroscopy* **171**, 186 (2016).
- [36] D. Pohl, S. Schneider, P. Zeiger, J. Rusz, P. Tiemeijer, S. Lazar, K. Nielsch, and B. Rellinghaus, *Scientific Reports* **7**, 934 (2017).
- [37] A. Edström, A. Lubk, and J. Rusz, *Physical Review Letters* **116**, 127203 (2016).

Supplementary Information: Induction Mapping of the 3D-Modulated Spin Texture of Skyrmions in Thin Helimagnets

S. Schneider

*Institute for Metallic Materials, IFW Dresden, Helmholtzstr. 20, 01069 Dresden, Germany and
Institut für Festkörper- und Materialphysik, Technische Universität Dresden, 01062 Dresden, Germany*

D. Wolf, B. Büchner, and A. Lubk

Institute for Solid State Research, IFW Dresden, Helmholtzstr. 20, 01069 Dresden, Germany

M. J. Stolt and S. Jin

*Department of Chemistry, University of Wisconsin-Madison,
1101 University Avenue, Madison, Wisconsin 53706, United States*

D. Pohl and B. Rellinghaus

*Institute for Metallic Materials, IFW Dresden, Helmholtzstr. 20, 01069 Dresden, Germany and
Dresden Center for Nanoanalysis, Technische Universität Dresden, 01062 Dresden, Germany*

M. Schmidt

*Department Chemical Metal Science, Max Planck Institute for Chemical
Physics of Solids, Nöthnitzer Str. 40, 01187 Dresden, Germany*

S. T. B. Goennenwein

*Institut für Festkörper- und Materialphysik, Technische Universität Dresden, 01062 Dresden, Germany and
Center for Transport and Devices of Emergent Materials,
Technische Universität Dresden, 01062 Dresden, Germany*

K. Nielsch

*Institute for Metallic Materials, IFW Dresden, Helmholtzstr. 20, 01069 Dresden, Germany and
Institute of Materials Science, Technische Universität Dresden, Helmholtzstr. 7, 01069 Dresden, Germany*

I. MAGNETIC HOLOGRAPHY

In off-axis electron holography the magnetic phase shift between the electron wave passing the object containing the skyrmions and the vacuum reference wave is given by the Aharonov-Bohm effect, i.e., by the magnetic flux enclosed between superimposing paths of the object and reference wave (e.g., [1]). Consequently, the spatial derivative of the reconstructed phase reads

$$\partial_{x,y}\varphi_{\text{mag}}(\mathbf{r}_{\perp}) = \frac{e}{\hbar}\partial_{x,y}\oint \mathbf{A}(\mathbf{r}) \, ds \quad (1)$$

$$= \frac{e}{\hbar}\partial_{x,y}\iint \mathbf{B}(\mathbf{r}) \, dS$$

$$= \frac{e}{\hbar}\int_{-\infty}^{\infty} \begin{pmatrix} B_y(\mathbf{r}_{\perp}) \\ -B_x(\mathbf{r}_{\perp}) \end{pmatrix} dz, \quad (2)$$

facilitating the computation of the projected magnetic fields. The last line of the above relation also holds in the case of Inline holography. To separate electric and magnetic phase shifts two images with flipped specimen are recorded [2]. Subtracting both allows to remove the electric phase shift, which is not changing sign under spatial inversion (as opposed to the magnetic one, which changes sign).

II. SAMPLE PREPARATION

Single crystals of FeGe were grown by chemical transport reaction. The transport experiment was carried out from the elements (Fe 99.998 % Alfa Aesar, Ge 99.9999 % Alfa Aesar) in an evacuated quartz tube in a temperature gradient from 580 °C (source) to 540 °C (sink). Iodine was used as transport agent. Selected crystals were characterized by EDXS, X-ray powder, and X-ray single crystal diffraction.

Fe_{0.95}Co_{0.05}Ge particles were fabricated by chemical vapor deposition process analogous to the one described in [3] used to form B20 FeGe nanowires. This CVD process, which was carried out at 550 °C, was adjusted slightly by the addition of ~ 100 mg of CoI₂ to the alumina source boat. This addition of CoI₂ resulted in both the small introduction of Co (<10%) into the final particles as well as the drastic change in morphology from nanowires to the slab-like particle shape.

III. OFF-AXIS HOLOGRAPHY RECONSTRUCTION

Fig. 1 depicts the object hologram, from which the object exit wave, amplitude and phase, is recon-

structured. The inset shows the hologram fringes within the $\text{Fe}_{0.95}\text{Co}_{0.05}\text{Ge}$ specimen with reasonable contrast of 5.5% at 1.4 nm fringe spacing ($6.6\text{ hologram pixels/fringe}$). The Fourier-based reconstruction involves fast Fourier transformation (FFT) of the hologram, centering and cutting out one sideband with a numerical mask (here: sinc-modulated square mask with 0.25 nm^{-1} edge length) and inverse FFT of the cut sideband. Furthermore, the phase image had to be unwrapped further to obtain the full phase shift larger than 2π , and the phase offset was set to zero in vacuum (lower right edge of the image).

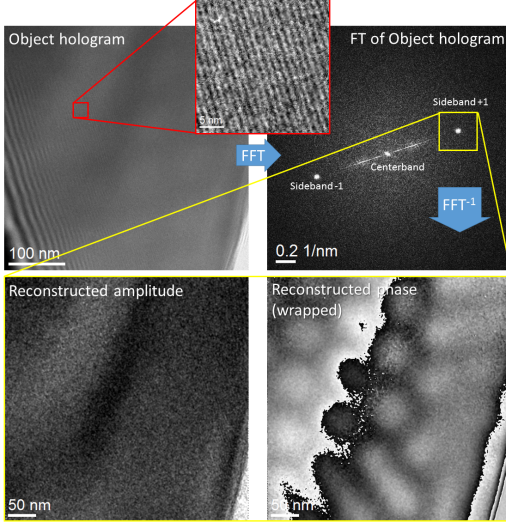


Figure 1. Object hologram reconstruction by Fourier method yielding the object exit wave, i.e., amplitude and phase image. Specimen: edge of a $\text{Fe}_{0.95}\text{Co}_{0.05}\text{Ge}$ particle.

IV. THICKNESS DETERMINATION

The object thickness was measured by evaluating zero-loss TEM micrographs with 10 eV energy slit width denoted here as I_{in} . In addition, unfiltered images were acquired to take into account the contribution stemming from elastical scattering denoted here as I_{el} . The thickness t over inelastic mean-free-path λ_{in} map can be computed using the relation

$$\frac{t(x, y)}{\lambda_{\text{in}}} = -\ln\left(\frac{I_{\text{in}}(x, y)}{I_{\text{el}}(x, y)}\right) \quad (3)$$

With the knowledge of $\lambda_{\text{in}} = 140\text{ nm}$ which we computed from the laws of plasmon scattering [4], we are able to determine a thickness map $t(x, y)$ as depicted in Fig. 2

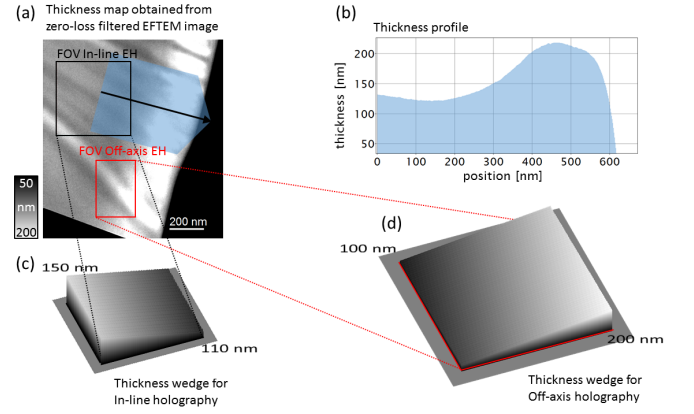


Figure 2. Thickness measurement from zero-loss filtered EFTEM image of the $\text{Fe}_{0.95}\text{Co}_{0.05}\text{Ge}$ particle which is investigated by electron holography. (a) Thickness map computed with Eq. 3. (b) Thickness profile towards the edge according to the arrow marked in (a). (c) Thickness wedge obtained by linear regression within the field of view (FOV) in in-line holography studies. (d) Thickness wedge obtained by linear regression within the field of view (FOV) for off-axis holography studies.

Likewise, the specimen thickness was determined exploiting the relation between the phase shift $\varphi(x, y)$ and the thickness distribution $t(x, y)$, i.e.,

$$\varphi(x, y) = C_E V_0 t(x, y) \quad (4)$$

with the interaction constant $C_E = 0.0065\text{ rad/Vnm}$ at 300 kV acceleration voltage and the mean inner potential (MIP) V_0 . The latter was determined to $V_0 = 13.4\text{ V}$ using, (i) isolated atomic potentials for Fe and Ge (parametrization of Weickenmeyer and Kohl [5]), (ii) a lattice constant of the cubic unit cell of 4.7 \AA , and (iii) two atoms per unit cell for Fe and Ge, respectively. The result shown in Fig. 3 reveals that the obtained thickness wedge (3(c)) deviates only by about 10 nm compared to the corresponding one obtained by EFTEM (Fig. 2(d)).

V. HOLOGRAPHIC TILT SERIES

In order to reveal a potential out-of-plane \mathbf{B} -field component of the helical phase in the $\text{Fe}_{0.95}\text{Co}_{0.05}\text{Ge}$ platelet, we investigated magnetic phase images recorded under different specimen tilt angles. The orientation of the tilt axis was chosen parallel to the propagation axis of the helical phase. We performed the following workflow:

1. Acquisition of hologram tilt series from -30° to $+39^\circ$ in 3° steps at room temperature (RT)
2. Acquisition of hologram tilt series from -30° to $+39^\circ$ in 3° steps at 90 K
3. Reconstruction of phase images from holograms

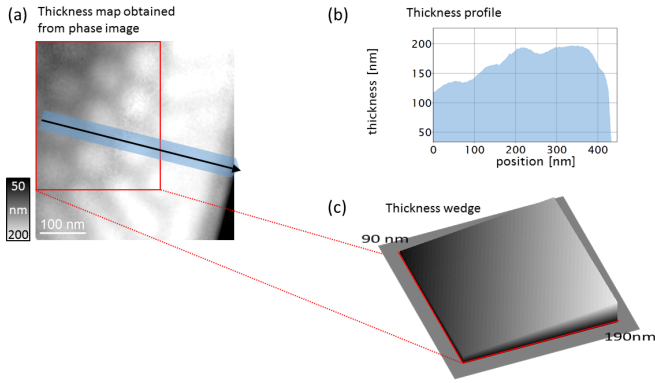


Figure 3. Thickness measurement from phase image of the $\text{Fe}_{0.95}\text{Co}_{0.05}\text{Ge}$ platelet which is investigated by electron holography. (a) Thickness map computed with Eq. 4. (b) Thickness profile towards the edge according to the arrow marked in (a). (c) Thickness wedge obtained by linear regression within the field of view (FOV) for off-axis holography studies.

4. Phase unwrapping and setting phase offset in the vacuum region of the phase image to 0 rad
5. Displacements correction of phase images within the tilt series, as well as between phase images at RT and 90 K
6. Calculation of derivatives of phase images in parallel (y -) direction to the tilt axis to obtain the projected B -component perpendicular to the tilt axis (B_x^{proj})
7. Calculation of thickness map from phase images at RT as explained in the previous section
8. Calculation of averaged B_x by

$$\bar{B}_x(x, y) = \frac{B_x^{\text{proj}}(x, y)}{t(x, y)}$$

In Fig. 4 holograms, reconstructed phase images, and the horizontal B -field component obtained by the above-mentioned workflow for a certain specimen tilt angle are depicted.

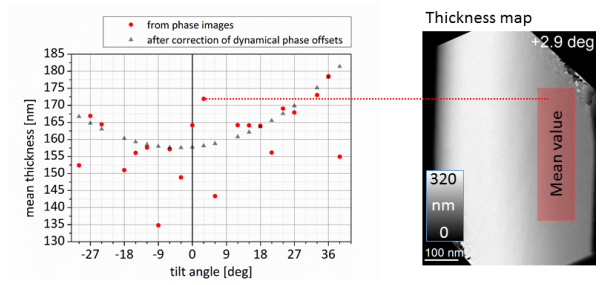


Figure 5. Projected thickness as a function of projection angle (sample orientation). The mean thickness was obtained in the region of the thickness map indicated by the red rectangle.

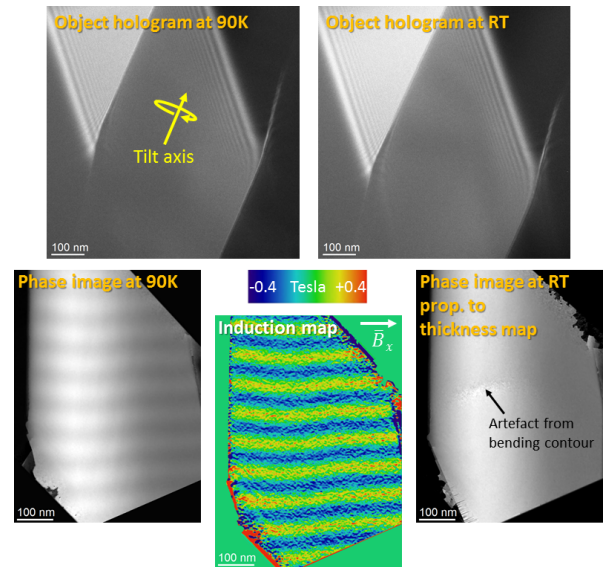


Figure 4. Holograms, reconstructed phase images, and obtained horizontal B -field component normalized thickness map of the $\text{Fe}_{0.95}\text{Co}_{0.05}\text{Ge}$ platelet at a tilt angle of -27° .

We encountered the problem that the phase images of the tilt series suffered from diffraction contrast, which lead to significant deviations in the phase signal and the determined thickness maps. Moreover, since bending contours caused by dynamical diffraction disturbed the phase images locally, the corresponding regions had to be excluded from the analysis. We tackled the first problem by plotting the projected thickness averaged over corresponding regions as a function of projection tilt angle, thereby identifying the “actual” trend of the projected thickness by a quadratic fit (Fig. 5). Note the negative systematic underestimation of the thickness at larger tilt angles.

VI. MAGNETIC INDUCTION MAPS

Fig. 6 shows representative magnetic induction maps of the tilt series after normalization with the corresponding thickness maps. It demonstrates that the helical

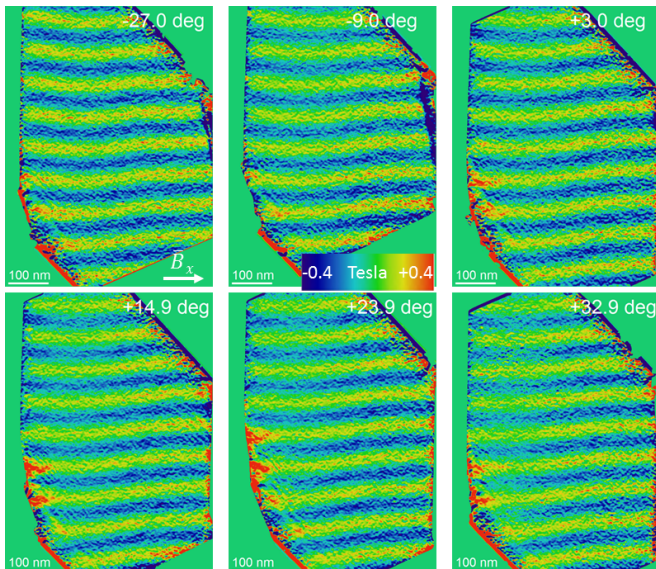


Figure 6. Induction maps of the $\text{Fe}_{0.95}\text{Co}_{0.05}\text{Ge}$ nanoplate in the helical phase taken at different tilt angles.

phase modulations are not straight but they are slightly bended in lateral direction. Since the thickness increases significantly towards the object edge on the left hand side (compare Fig. 5 right), a possible explanation of this bending could be an underlying modulation in depth (z) direction.

VII. MAGNETOSTATICS

The saturation magnetization of a $\text{Fe}_{0.95}\text{Co}_{0.05}\text{Ge}$ powder measured by SQUID amounts to

$$M_s = 3.45 \times 10^5 \frac{\text{A}}{\text{m}}. \quad (5)$$

From that we may derive the maximal magnetic induction expected in the z -invariant spin modulation by taking into account that Bloch like spin modulations are magnetic charge free. With no in-plane applied field this yields

$$B_{\perp, \max} = \mu_0(M + H) \quad (6)$$

$$\stackrel{H=0}{=} 4\pi \times 10^{-7} \frac{\text{Vs}}{\text{Am}} \cdot 3.45 \times 10^5 \frac{\text{A}}{\text{m}} = 0.43 \text{ T}.$$

For the quantitative simulation of the complete magnetic field distribution (and hence the projected fields) in and around a thin slab of FeGe carrying a 3D modulated helical or Bloch Skyrmion texture we solved the well-known system of magnetostatic equations

$$\begin{aligned} \nabla \mathbf{M} &= \Delta \Phi_M \\ \mathbf{H} &= \nabla \Phi_M \\ \mathbf{B} &= \mu_0(\mathbf{H} + \mathbf{M}) \end{aligned} \quad (7)$$

with a scalar potential Φ_M numerically. More specifically, we started out by setting up a 3D magnetic texture \mathbf{M} including various surface modulations, i.e., chiral surface twist, and z -dependent shifts. Subsequently, we computed the scalar magnetic potential Φ_M , the magnetic field strength \mathbf{H} and finally the magnetic induction \mathbf{B} . The differential equations involved are solved in Fourier space, which implies that periodic boundary conditions have been assumed. In order to suppress artefacts due to this choice of boundary conditions, our computations have been carried out in a sufficiently large supercell containing the slab. To compare the simulation with the experimentally reconstructed projections of the \mathbf{B} -field under different tilt angles, we numerically integrated the magnetic induction into the corresponding directions.

-
- [1] Hannes Lichte, Felix Börrnert, Andreas Lenk, Axel Lubk, Falk Röder, Jan Sickmann, Sebastian Sturm, Karin Vogel, and Daniel Wolf. Electron holography for fields in solids: Problems and progress. *Ultramicroscopy*, 134:126–134, nov 2013. ISSN 03043991. doi:10.1016/j.ultramic.2013.05.014. URL <http://www.sciencedirect.com/science/article/pii/S0304399113001332>.
- [2] Takeshi Kasama, Rafal E., and Marco Beleggi. Electron Holography of Magnetic Materials. In *Holography - Different Fields of Application*. InTech, sep 2011. doi:10.5772/22366. URL <http://www.intechopen.com/books/holography-different-fields-of-application/electron-holography-of-magnetic-materials>.
- [3] Matthew J. Stolt, Zi-An Li, Brandon Phillips, Dongsheng Song, Nitish Mathur, Rafal E. Dunin-Borkowski, and Song Jin. Selective Chemical Vapor Deposition Growth of Cubic FeGe Nanowires That Support Stabilized Magnetic Skyrmions. *Nano Letters*, 17(1):508–514, jan 2017. ISSN 1530-6984. doi:10.1021/acs.nanolett.6b04548. URL <http://pubs.acs.org/doi/abs/10.1021/acs.nanolett.6b04548>.
- [4] Rf Egerton. *Electron energy-loss spectroscopy in the electron microscope*. Plenum Press, 1996. ISBN 9781441995827. doi:10.1007/978-1-4419-9583-4. URL https://books.google.de/books/about/Electron{ }Energy{ }Loss{ }Spectroscopy{ }in{ }the.html?id=ieMqIzeHdC4C{ }&redir{ }_esc=y.
- [5] A. Weickenmeier and H. Kohl. Computation of absorptive form factors for high???energy electron diffraction. *Acta Crystallographica Section A*, 47(5):590–597, sep 1991. ISSN 16005724. doi:10.1107/S0108767391004804. URL <http://scripts.iucr.org/cgi-bin/paper?S0108767391004804>.